THE AMERICAN SOCIETY OF MECHANICAL ENGINEERS
345 E. 47th St., New York, N.Y. 10017

94-GT-236

DESIGN OF A LOW ASPECT RATIO TRANSONIC COMPRESSOR STAGE USING CFD TECHNIQUES

Nelson L. Sanger
NASA Lewis Research Center
Cleveland, Ohio

ABSTRACT

A transonic compressor stage has been designed for the Naval Postgraduate School Turbopropulsion Laboratory. The design relied heavily on CFD techniques while minimizing conventional empirical design methods. The low aspect ratio (1.2) rotor has been designed for a specific head ratio of .25 and a tip relative inlet Mach number of 1.3. Overall stage pressure ratio is 1.56. The rotor was designed using an Euler code augmented by a distributed body force model to account for viscous effects. This provided a relatively quick-running design tool, and was used for both rotor and stator calculations. The initial stator sections were sized using a compressible, cascade panel code. In addition to being used as a case study for teaching purposes, the compressor stage will be used as a research stage. Detailed measurements, including non-intrusive LDV, will be compared with the design computations, and with the results of other CFD codes, as a means of assessing and improving the computational codes as design tools.

NOMENCLATURE

c_p specific heat at constant pressure
D diffusion factor
P pressure
PR pressure ratio, total-to-total
R gas constant
s entropy
T temperature
U rotor wheel speed
V velocity

$\bar{W}$ specific weight flow ρV
β flow angle
γ ratio of specific heats
δ deviation angle $\beta_2 - \kappa_2$
i incidence angle $\beta_1 - \kappa_1$
κ blade metal angle
ρ gas density
σ blade solidity , chord/blade spacing
Ψ specific headrise
ϖ total pressure loss coefficient

Superscripts:

$'$ relative

Subscripts:

O total
1 inlet
2 outlet
is isentropic process value
t tip

INTRODUCTION

The Naval Postgraduate School axial transonic compressor stage and test facility were designed in 1968 by Prof. Michael H. Vavra. The purpose of the stage was to provide an advanced test vehicle for operational and research experience for naval officers. The completed design, aerodynamic and mechanical, was performed manually by Prof. Vavra, a notable accomplishment. However, in almost the last step in the design calculations, an error in sign occurred which resulted in an erroneous radial distribution of blade setting angle. This distribution was built into the rotor. A second inaccuracy arose from an assumption made for the through flow into the rotor. These, and other aspects of the Vavra design are described by Erwin (1983).

Presented at the International Gas Turbine and Aeroengine Congress and Exposition
The Hague, Netherlands — June 13–16, 1994
This paper has been accepted for publication in the Transactions of the ASME
Discussion of it will be accepted at ASME Headquarters until September 30, 1994

The major effect of the design errors occurred over the outer 25% of span, where the rotor blade setting angles were more open than the design intent, and over the inner 25% of span where the incidence was again too high because axial velocities were lower than had been assumed. The higher resulting incidence angles toward the tip increased supersonic expansion around the leading edge, producing larger shock losses and lower pressure rise than design intent. This, and the higher incidence angles toward the hub, led to a radial distribution of flow angle from the rotor which was not matched to the distribution used in the design of the stator. Experimental results for the stage, and for the rotor only, were reported by Neuhoff (1985 & 1986).

While the Vavra stage design was not a correct one, it was quite successful in that it facilitated the development of a transonic compressor test capability at the Naval Postgraduate School, and of the development of high response instrumentation techniques to determine flow behavior in transonic stages (Shreeve & Neuhoff, 1984 and Neuhoff et al, 1986). However, a new stage design was sought, one for which detailed measurements would provide a meaningful evaluation of current design and analysis methods. NASA Lewis Research Center agreed to perform the aerodynamic and mechanical design of such a stage. This provided the opportunity to use the newly-emerging CFD tools, supplemented by traditional methods and, later, to have the procedure tested against experimental results. The purpose of the present paper is to present the design that was obtained, with a description of the design/analysis process that was used to arrive at the final geometry.

TEST FACILITY

The open loop test facility and present compressor stage is shown in Figure 1. Air enters through filters in a housing which surrounds the inlet piping. Within the housing an intake throttle valve is attached to a settling chamber. The throttle valve consists of two plates having identical hole patterns; the plates rotate with respect to each other and are driven by an hydraulic actuator. The flow then passes through perforated plates in the 0.813-meter (32-inch) diameter settling chamber; following the settling chamber, the flow passes into a 0.457-meter (18-inch) diameter pipe in which there is a calibrated nozzle. The flow enters the compressor through a 0.279-meter (11-inch) diameter inlet pipe and exits radially. A honeycomb section following the stator removes any circumferential velocity component from the flow. Thus the torque supplied to the rotor is equal to the torque experienced by the stator and honeycomb section. The stator section is mounted on ball races and is free to rotate against flexures instrumented with strain gauges. The strain gauge reading is then a measure of the torque supplied to the rotor.

The compressor rotor is driven by an opposed-rotor single stage air turbine supplied by air from the laboratory compressed air supply. The compressed air is supplied to the laboratory by a 12-stage Allis-Chalmers axial compressor.

DESIGN PROCEDURE

Preliminary Design. Design goal was to achieve as high a loading and specific weight flow as was practical, while keeping rotor tip Mach number at a moderate level. Chief constraint was power available from the drive turbine. The results of a parametric study are shown in Figure 2. Specific head-rise was calculated for a series of tip speeds and pressure ratios

($\Psi = c_p T_{01} (PR^{(\gamma-1/\gamma)} - 1) / U_t^2$). After consideration of various configurations, a target design was specified which has higher loading and lower tip speed than the original Vavra design. The loading is also slightly higher than the NASA Rotor 67, which is also plotted on Figure 2.

The power required by the target design (341 kw) was set very near the available (limiting) power available from the turbine drive (354 kw). To minimize fabrication expenses, the external flow path and stator mechanical design was retained. This restricted aerodynamic design choices, but was considered necessary for economic reasons. A new conical spinner for the rotor was designed having a constant 28-degree ramp angle. This angle is effectively set by the choice of pressure ratio and aspect ratio.

A review of in-house and contractor designs led to the choice of an approximately constant radial distribution of exit total pressure; exit total temperature (energy addition) was chosen to be nearly radially constant, but higher in the tip region to compensate for shock losses (see figure 16 later). These distributions of total pressure and temperature, the overall pressure and temperature ratio, flow rate and the new flow path were entered into a streamline curvature design program. During the preliminary design process, before final design parameters were chosen, various combinations of parameters were assessed until detailed distributions of parameters such as diffusion factor ($D = 1 - V_2'/V_1' + \Delta V_\theta'/2\sigma V_1'$) and loss appeared reasonable in light of contemporary experience. Specific empirical loss sets or deviation angle distributions were not used. Deviation angle estimates for the controlled-diffusion stator were based on experimental results from the controlled-diffusion stator designed by Sanger (Sanger, 1982) and tested at the Naval Postgraduate School cascade facility.

A summary of the design parameters is given in Table I.

Computer Codes. Several computer codes were used in the design process.

Streamline-curvature: The NASA in-house streamline-curvature code was used for preliminary calculations and production of fabrication coordinates. The main-frame version of the code was documented in NASA TP-1946 (Crouse & Gorrell, 1981). An improved PC-version, available from and supported by James E. Crouse, was used in this design. This version has shown less sensitivity to blade section stacking in high hub ramp angle cases as encountered in this design. Steady, axisymmetric flow is assumed, thus reducing the problem to solving the two-dimensional flow in the meridional plane. The full radial equilibrium equation forms the basis of the code. The aerodynamic solution gives velocity diagrams on selected streamlines of revolution at the blade edges. There are no calculation stations inside the blade row. There are numerous options for controlling the form of input and for specifying the amount of output.

Blade-element code: The geometry portion of the streamline-curvature code has been extracted and combined with in-house graphics to run on the Lewis main-frame computer. This short code affords a convenient means for designing individual blade sections according to the criteria established in the streamline-curvature code.

The meanline of the blade is described by two polynomial segments, each of which can be specified by up to a quartic polynomial. The polynomial is a fit of local blade angle against mean-line distance. The distribution of blade thickness about the mean-line is also specified by two polynomials, each of which may be quartics. The thickness is added symmetrically on either side of the mean-line. A more complete description of this process is given by Sanger (1982).

Denton TIP3D: The 3D analysis code employed was a hybrid code developed by Denton and named TIP3D. It was originally reported in 1986 (Denton, 1986), but has since been expanded and upgraded. It uses the original Denton Euler code as a base (Denton, 1982), but couples it with a relatively simple viscous approximation in order to account for blockage and secondary flow effects. In the approximation, viscous effects are taken into account by including a body force term in the momentum equation and a source term in the energy equation. Wall shear stress is approximated by an empirical equation. The distribution of shear stress from the wall is obtained from the Boussinesq eddy viscosity model. The viscous effects can be "cut off" at some fraction of passage width by providing that fraction as input. With sufficient grid points within the boundary layer one can obtain a reasonably good prediction of the flow in a real turbulent boundary layer, and at a considerable saving in computing time and cost.

An additional improvement to the original code is the inclusion of tip clearance flow. The code is not capable of calculating the details of the flow in a tip clearance region, but is capable of including the effect on the primary flow and on the overall performance. The leakage is predicted simply by reducing the blade thickness to zero in the clearance gap, and by applying a periodicity condition within the gap in exactly the same way periodicity is applied upstream and downstream of the blade row. This enables flow to pass over the blade tip, and ensures that no load is carried within the gap. A typical run time for a transonic rotor blade row was 20 minutes on a Cray YMP.

Panel Code: Because the stator flow field is subsonic, a subsonic 2D panel code was used to screen blade sections. The entire stacked 3D stator was then analyzed by the TIP3D code. The panel code (McFarland, 1984), employs a surface singularity method which solves the inviscid, irrotational, compressible blade-to-blade flow equations on a surface of revolution. Streamsheet thickness can be incorporated as a function of meridional distance. The governing equations are linearized by approximating compressibility effects, and solved using an integral technique (panel method).

Blade sections were created with the blade geometry code and analyzed with the panel code and an integral boundary layer code (described below). This provided a quick screening method and allowed development of a series of blade sections which showed no boundary layer separation at the design point. A typical run time on a 386 PC (25 MHZ CPU) is 30 seconds.

Boundary Layer Code: An integral boundary layer code (McNally, 1970) was used in conjunction with the panel code to screen the 2D blade sections. The design point surface velocity distributions calculated by the panel code were entered into the boundary layer code and the condition of the turbulent boundary layer was monitored. No blade section was accepted which indicated that turbulent separation had occurred (incompressible form factor must be less than 2.0)

The McNally code uses integral methods to solve the two-dimensional, compressible laminar and turbulent boundary layer equations in an arbitrary pressure gradient. Cohen and Reshotko's (1956) method is used for the laminar boundary layer, transition is predicted by the Schlichting-Ulrich-Granville (Schlichting, 1979) method, and Sasman's and Cresci's (1966) method is used for the turbulent boundary layer. A typical run time on the Lewis Amdahl 5870 main-frame running under the VM operating system is 10 seconds.

Rotor Design. Velocity triangles were set with the streamline curvature code. Blade shapes were then fitted to the triangles using both quasi-3D and full-3D calculations. Rotor tip solidity was set at 1.3. At that solidity and a tip inlet Mach relative number of 1.3, it was verified that the leading edge oblique shock would be contained in the blade passage, striking the suction surface at about 80 to 90 percent of chord. The radial distributions of inlet relative Mach number and of D-Factor for the rotor are shown in Figure 3.

Initially, rotor blade sections were screened using a quasi-3D version of the Denton Euler code which had a transpiration model to simulate the boundary layer blockage. Surface boundary layer condition was checked using the McNally integral boundary layer code. Criteria used for design were to minimize supersonic acceleration on the uncovered portion of the blade to reduce shock strength, and then to control diffusion in the covered portion to prevent or delay boundary layer separation.

This procedure provided a quick, initial screening of blade shapes, but with the advent of the full-3D code with body forces, it probably would be more effective to use the 3D code and develop a 3D geometry package to fit and stack tentative blade designs. Although a quasi-3D code is quick, the result may be inaccurate because transonic sections are quite sensitive to streamtube height, a user-specified quantity.

When the 3D body force code became available, the blade sections originally defined using the quasi-3D code were used as a base design; subsequent alterations to the geometry were made based on the 3D calculations. Three blade sections from the final design are shown in Figure 4. Leading edge radii non-dimensionalized by chord varied from .002 at the tip to .0058 at the hub (Fig. 5). Trailing edge radius to chord had a similar distribution. Maximum thickness followed a linear variation from 3-1/2 % of chord at the tip to 8 % of chord at the hub. The rotor leading edge wedge angles in the supersonic region of the blade were minimized by positioning the maximum thickness location well back on the blade. The maximum thickness location was varied from 76 % of chord at the tip to 50 % at the hub (Fig. 6).

A meridional view of the grid used in the full-3D calculations is shown in Fig. 7. Slightly more than 100,000 points were used, with 97 points in the meridional direction and 33 each in the radial and circumferential planes. The grid points were packed close to the blade surfaces, hub and casing, and meridionally from the leading and trailing edges of the blades using a geometric packing scheme. Expansion factors were 1.25 in the spanwise direction, 1.3 in the blade-to-blade direction, 1.25 in the meridional direction upstream and downstream of the blades, and 1.1 from the blade leading and trailing edges in the meridional direction inside the blade passage.

A complete calculated rotor map is presented in Figure 8. The calculated performance projects a pressure ratio of 1.61 at design

flow and an adiabatic efficiency of 90.1% At the best efficiency flow point the pressure ratio was 1.58 and efficiency was 90.3%. Recalculating the performance with no tip clearance (at a different flow rate) raised the efficiency by about 2 points. Performance was calculated for decreasing flow (approaching stall). As the flow decreased the number of time steps required for the solution to converge increased until the solution failed to converge. The nearest-stall points plotted in Figure 8 are for converged or nearly converged points. Whether these points correspond to actual stall is open to question, and must await experimental investigation. All that can be said is that numerically convergent solutions were obtained (albeit at increased numbers of time steps).

Relative Mach number contours are presented in Figure 9 for the design flow point. Meridional planes 5 % of passage width from the pressure and suction surfaces are shown in Figure 9a and b respectively, and blade-to-blade planes at 15, 50 and 85 % span from tip are shown in c, d, and e respectively. A weak oblique shock reflects from the suction surface as a strong normal shock at about 85 % chord (Fig. 9c). The shock becomes weaker and disappears as the hub is approached. The tip clearance flow is evident (Fig. 9b). The spacing between the casing and the first gridline represents a distance of 0.18% of blade span, which is equivalent to an average tip clearance of .0114 cm (.0045 in.). The cold clearance of the existing Vavra rotor is .0254 cm (.010 in.). If built to the same specifications, the subject rotor should be expected to have a hot, running clearance reasonably close to the value used in the 3D calculations.

At the near stall point the normal shock is pushed forward in the passage and stands in front of the leading edge, intersecting the suction surface at about 30 % chord near the tip. The three-dimensional spanwise sweep of the normal shock is clear from the meridional view near the suction surface (Fig. 10b).

At the near choke point the normal passage shock has moved to the rear of the passage and extends to within 15 % of the hub plane. There is still some sweep to the shock, but less than was present at the other flow conditions (Fig. 11b).

Losses are well-behaved at the design point. Entropy function contours, $\exp(-\Delta s/R)$, are presented in Fig. 12 for the cross-channel plane just upstream of the trailing edge. The losses on the suction surface are higher than the losses on the pressure surface due to the combined effect of shock losses and higher diffusion. The considerable effect of the tip clearance flow is evident from Fig. 13 which shows losses on a meridional plane mid-way between blade surfaces. Entropy contours on the blade surfaces are shown in Fig. 14. Losses are high in the wakes as expected, with some indication of limited boundary layer separation near the trailing edge.

At the near stall flow the suction surface boundary layer is quite thick (Fig. 15) and tip clearance effects have penetrated into the core flow. Losses are higher, but are concentrated mainly in blade wakes and near the casing.

Aerodynamic quantities were mass-averaged in the blade-to-blade plane and selected parameters are plotted in Fig. 16 as conventional radial distributions of performance quantities. The radially constant design energy addition and total pressure are clear from Fig. 16a and 16b. Losses ($\overline{\omega} = (P'_{02is} - P'_{02}) / (P'_{01} - p_1)$), as expected, are concentrated in the endwall regions with the casing having the greatest concentration of losses due to tip clearance flow and shock losses. Deviation angle distribution was initially set using Carter's Rule, but evolved to the final distribution (Fig. 16e) as a result of engineering judgements made in the course of analyzing the computations. Incidence angle distributions (Fig. 16d) evolved similarly. Area margin considerations were not ignored, but results of the computations drove the choice of setting angle and mean camber distribution rather than empirical rules. For reference, tip region throat area margins ((A/A*) - 1) were about three percent.

At near stall, energy addition and losses are high in the tip region because high incidence angles lead to high supersonic expansion and shock losses. Exit total pressure is also higher over the outer portion of the span.

Stator Design. The stator poses some special problems. At design flow, inlet Mach number at the hub is 0.7 and diffusion factors are greater than 0.5 over the entire span, reaching .58 at the hub (Fig. 17). Camber angles range from 51 to 57 degrees. Chord was kept radially constant to permit exchanging the new stator for the old. Twenty seven blades were selected, giving a hub solidity of 1.5. A controlled-diffusion blade shape with elliptical leading and trailing edges was used. The maximum thickness distribution is shown in Figure 18; the position of maximum thickness is constant from hub to tip at a value of 47 percent of chord. The blade section at mid-span is shown in Fig. 19, and is typical of blade shapes at other sections. A typical surface velocity distribution is given in Figure 20. Because the stator is free to rotate in order to measure torque supplied to the rotor, there is a clearance region between the tip and the casing; this region was accounted for in the 3-D computations.

Velocity triangles were set using a combination of the streamline curvature calculations and rotor exit profiles from 3-D computations. A screening process was followed which aimed to produce a blade which was separation-free. The blade-element code was used to define a blade, surface Mach numbers were computed with McFarland's quasi-3D panel code, and the boundary layer was computed with the McNally integral boundary layer code. Adjustments were made to the geometry and the process was repeated until no separation of the suction surface boundary layer was predicted (incompressible form factor less than 2.0). A controlled diffusion shape was used, which strives for an acceleration to a peak Mach number on the suction surface followed by a rapid deceleration which reduces in magnitude as the trailing edge is approached. In highly loaded blades such as these, it is necessary to control the deceleration from the leading edge on the pressure surface of the blade as well. The mid-span blade section was sized first and then a similar process was applied to blade sections at 15, 30, 70, and 85 percent of span. The blade was stacked in the streamline curvature code and geometric coordinates generated for the Denton 3-D computation. Because of time considerations, the Denton code was used only for post-design analysis. A "conventional" controlled diffusion stator was designed. That is, no attempt was made to customize it for end-wall flows (end bends) nor for high Mach numbers at the hub (leading edge sweep). Such customizing will be left for a future design, if attempted.

A 3-D grid identical to that applied to the rotor (Fig. 7) was generated for the stator. The tip clearance flow passes between the casing and the first grid line, amounting to a tip clearance gap of 0.18 percent of span. This is equivalent to an average clearance of

.00838 cm (.0033 in.). The present Vavra stator has a cold clearance of .0229 to .0254 cm (.009 to .010 in.). If the subject stator is built to the same specifications, the actual tip clearance (accounting for thermal expansion) may be twice the value used in the 3D calculations.

Absolute Mach number contours in the blade-to-blade plane are presented in Fig. 21 at the design point flow for cascade sections at 15, 50 and 85 % span from the hub. Peak Mach numbers occur, as expected, about one-third of chord from the leading edge, and rapidly diffuse. Mach number levels are the highest in the hub region. The entropy plots (Fig. 22) show a thickening of the boundary layer and perhaps some separation of the boundary layer at the hub and tip elements. The cross-plane entropy plots (Fig. 23) show the development of the surface boundary layers to be relatively well-behaved. However, the stator must accept flow with high loss in the tip region and, due to its own tip clearance flow, contributes further losses near the suction surface extending inward over 15 to 20 % of span. Secondary flow in the hub region places an accumulation of low energy flow near the trailing edge adjacent to the suction surface, and the high loss region extends over 10 to 15 percent of span. Figure 24 provides another perspective on the distribution of loss, showing losses on a meridional plane 5% of blade gap from the suction surface. The effect of the tip clearance flow is evident.

At the near stall point the entropy contours in the blade-to-blade planes (not shown) indicate blade suction surface boundary layers are separated from the leading edge. Losses are concentrated along the suction surface and in the corners between the suction surface and the endwalls (Fig. 25). The tip clearance flow interacting with the separated surface boundary layer provides a large concentration of losses. From the results of this calculation it would be expected that the stator will control the stall margin of the stage.

As with the rotor, aerodynamic quantities were mass-averaged in the blade-to-blade plane. Parameters of interest are plotted in Fig. 26 for the design flow condition. The calculated performance nearly achieves the intended constant radial distribution of total pressure. The combination of low energy inlet flow from the rotor plus the effect of stator tip clearance flow act to increase the losses over the outer span and reduce the exit total pressure in this region. The net effect of these losses is to reduce stage efficiency to 83 % at design flow. A re-calculation with zero stator tip clearance flow resulted in a stage efficiency gain of only 0.4 points to 83.4 %. The combined effect of shock losses, boundary layer growth, and tip clearance in the rotor significantly affects the inlet flow to the stator in the tip region. Obviously, some form of re-staggering should have been employed in the outer span region of the stator.

At near stall the mass-averaged losses are significant over the outer half of the flow path and reduce the exit total pressure correspondingly. Incidence angle is elevated in the outer region by the deficit in flow velocity in this high loss region. Deviation does not appear to change much between design flow and near stall - a worthy subject-area for experimental confirmation.

Mechanical Design. The mechanical adequacy of the rotor, stator, and new nose cone was evaluated. Material chosen for the rotor was a high strength Aluminum alloy, 7050-T7651, and for the stator a slightly lower strength Aluminum alloy, 7075-T7351. Combined stress from centrifugal and bending loads for the rotor was calculated with NASTRAN. A maximum stress under combined loads was found to be 281.4 megaPa, which is below the allowable stress of 322 megaPa (obtained by applying a 1.5 safety factor to the ultimate stress). A maximum untwist of 1.5 degrees was calculated, and the cold coordinates were corrected to account for this.

NASTRAN was also used to determine mode shapes and natural frequencies over a speed range of 0 to 35,000 rpm. Results are shown in a Campbell Diagram (Fig. 27). The only resonances of significance occur in first bending mode at third and fourth engine orders. The engine orders and the speeds involved (less than 70% of design speed) are unlikely to be a source of forced vibration problems. A rotor high cycle fatigue analysis was performed and plotted as a Modified Goodman Diagram. The outcome indicated acceptability of the material at design speed and marginal acceptance at 110% design speed. The use of generous safety factors in the analysis, coupled with a clean inlet flow environment would suggest no cause for concern. The rotor was also analyzed for subsonic stall flutter in bending and torsional modes by a reduced velocity parameter analysis. In each case the reduced velocity parameter was less than the allowable limit (0.8 vs. 1.25 in torsion and 2.3 vs. 6.6 in bending).

The stator was also subjected to a NASTRAN blade stress analysis. Deflection was small and the maximum stress of 124.8 megaPa was well below the allowable stress of 303.4 megaPa. Mode shapes and natural frequencies were determined for the stator by a NASTRAN analysis. A Campbell Diagram was prepared and showed no excitations below the 5th engine order, but the 22nd engine order (rotor blade count) did show a third mode crossing (a combined bending and torsion) at 85% of design speed, and may bear watching. A subsonic stall flutter analysis was also performed on the stator; the reduced velocity parameter in torsion was 0.4, well below allowable of 1.25. (There were no pure bending modes indicated for the stator). A finite element stress analysis was conducted on the new nose cone and on the rotor hub. Maximum stress on the nose cone was 88.95 megaPa and on the rotor hub, 79.3 megaPa, well below allowable stress levels. Finally, a shaft critical speed analysis was performed on the shaft assembly with the new nose cone. The first rigid shaft critical speed of the system was 37,358 rpm, well above the design speed of 27,085 rpm.

SUMMARY OF RESULTS

1. A transonic compressor stage has been designed for the Naval Postgraduate School Turbopropulsion Laboratory. The low aspect ratio (1.2) rotor has a specific head-rise of 0.25 and a tip relative Mach number of 1.3. Overall stage pressure ratio is 1.56. The design relied heavily on CFD techniques rather than conventional empirically-based methods.

2. An Euler code augmented by a distributed body force model to account for viscous effects was used heavily in the rotor design. Predicted total pressure ratio at design flow is 1.61 at an efficiency of 90.1%. At the best efficiency flow the pressure ratio is predicted to be 1.58 at an efficiency of 90.3%. Losses at design flow were concentrated in the end wall regions, particularly at the tip where shock loss and tip clearance effects were significant.

3. The stator was designed with controlled-diffusion blade shapes using a 2D panel method and integral boundary layer method. Three-dimensional analysis indicates that the design could have benefitted from re-staggering in the tip region (end bends) because

of the low energy flow ingested from the rotor. At design flow, predicted stage pressure ratio is 1.56 at an efficiency of 83%. Diffusion factors are greater than 0.5 over the entire stator span. The 3D calculations at off-design suggest that the stator will control stalling flow for the stage.

4. Although tip clearance effects are not modeled in detail in the 3D calculation method, tip clearance flow and its effect on performance is modeled. For the rotor, the effect of tip clearance was demonstrated to cost 2 points in efficiency. The stator is free to rotate in order to measure torque supplied to the rotor and, therefore, also has a tip clearance. In the case of the stator, clearance flow is driven only by the pressure gradient across the blade (no scraping flow and associated vortex), and the calculated deficit in performance was only 0.4 points in efficiency.

5. High strength Aluminum alloys were chosen for rotor and stator, and both blade rows were analyzed using NASTRAN. Calculated stresses were all within allowable limits; a Campbell diagram for the rotor indicated the only significant resonance occurs in first bending mode at 3rd and 4th engine orders, and at speeds below 70% of design speed; the stator Campbell diagram shows a third mode crossing at 22nd engine order (rotor blade count) at 85% design speed. This is not considered serious, but will bear watching. Subsonic stall flutter analyses indicated both rotor and stator to be within safe limits.

ACKNOWLEDGEMENTS

The author would like to thank Mr. Donald Sandercock (NASA-Lewis, retired) for his advice and counsel, Dr. Lonnie Reid (NASA-Lewis) for his support, Mr. Tony Herrmann (NASA-Lewis) for overseeing the mechanical design activities, and Mr. James E. Crouse (Dresser-Rand) for his assistance and counsel.

REFERENCES

Cohen, C. B., and Reshotko, E., 1956, "The Compressible Laminar Boundary Layer with Heat Transfer and Arbitrary Pressure Gradient," NACA TR-1294.

Crouse, J. E., and Gorrell, W. T., 1981, "Computer Program for Aerodynamic and Blading Design of Multistage Axial-Flow Compressors," NASA TP-1946.

Denton, J. D., 1982, "An Improved Time-Marching Method for Turbomachinery Flow Calculation," ASME Paper 82-GT-239.

Denton, J. D., 1986, "The Use of a Distributed Body Force to Simulate Viscous Effects in 3D Calculations," ASME Paper 86-GT-144.

Erwin, J. R., 1983, "A Review of the Design of the NPS/TPL Transonic Compressor," Contractor Report NPS67-83-004CR, Naval Postgraduate School, Monterey, CA.

McFarland, E. R., 1984, "A Rapid Blade-to-Blade Solution for Use in Turbomachinery Design," J. of Engineering and Power for Gas Turbines, vol. 106, no. 2.

McNally, W. D., 1970, "Fortran Program for Calculating Compressible Laminar and Turbulent Boundary Layers in Arbitrary Pressure Gradients," NASA TN D-5861.

Neuhoff, F., 1985a, "Modifications to the Inlet Flow Field of a Transonic Compressor Rotor," Contractor Report NPS67-85-008CR, Naval Postgraduate School, Monterey, CA.

Neuhoff, F., 1985b, "Investigation of the Interaction Between the Rotor and Stator of a Transonic Compressor," Contractor Report NPS67-85-011CR, Naval Postgraduate School, Monterey, CA.

Neuhoff, F., Shreeve, R. P., and Fottner, L., 1986, "Evaluation of the Blade-to-Blade Flow from a High Speed Compressor Rotor," ASME Paper 86-GT-117.

Sanger, N. L., 1983, "The Use of Optimization Techniques to Design Controlled-Diffusion Compressor Blading," J. of Engineering for Power, Vol. 105, pp. 256 - 264.

Sasman, P. K., and Cresci, R. J., 1966, "Compressible Turbulent Boundary Layer with Pressure Gradient and Heat Transfer," AIAA Journal, Vol. 4, No. 1.

Schlichting, H., 1979, "Origin of Turbulence II," *Boundary Layer Theory*, 7th ed., McGraw-Hill, New York.

Shreeve, R. P., and Neuhoff, F., 1984, "Measurements of the Flow from a Compressor Rotor Using a Dual-Probe Digital Sampling (DPDS) Technique," J. of Engineering for Gas Turbines and Power, Vol. 106, no. 2.

Rotor Pressure Ratio	1.61
Stage Pressure Ratio	1.56
Tip Speed	396.2 m/sec (1300 ft/sec)
Design Weight Flow	7.75 kg/sec (17.09 lb-m/sec)
Specific Weight Flow	170.9 kg/sec-m^2 (35 lb-m/sec-ft^2)
Specific Head Rise	0.246
Tip Inlet Relative Mach Number	1.28
Aspect Ratio	1.2
Hub/Tip Radius Ratio	0.51
Number of rotor blades	22
Number of stator blades	27
Tip Solidity - Rotor	1.3
Tip Solidity - Stator	1.0
Outside Diameter	27.94 cm (11.0 in)
Rotor Diffusion Factor - tip	0.4
Rotor Diffusion Factor - hub	0.47
Stator Diffusion Factor - tip	0.52
Stator Diffusion Factor - hub	0.58

Table I - Design Parameters

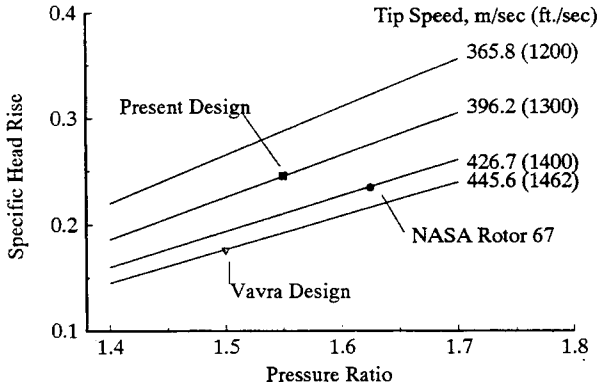

Fig. 2 Specific Head Rise

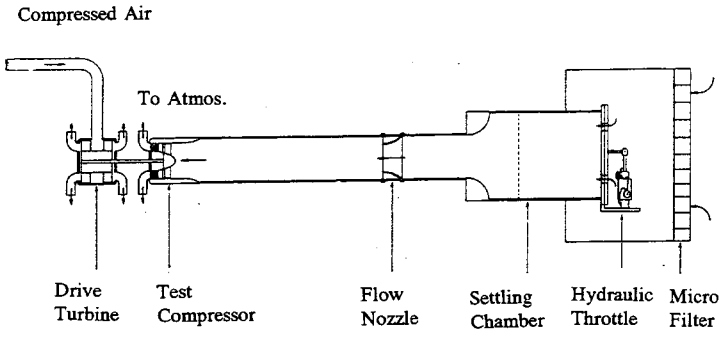

(a) Test facility and piping (not to scale)

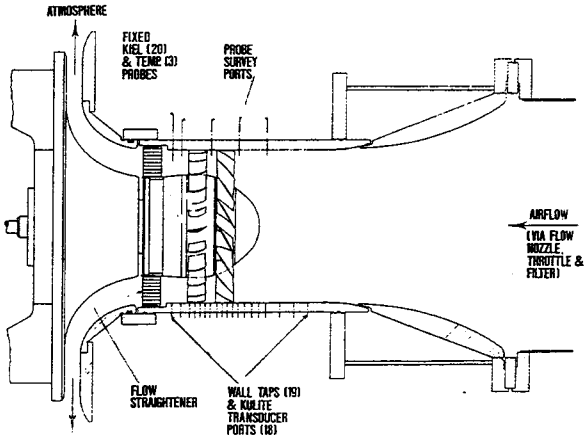

(b) Exisiting transonic stage (Vavra design)

Fig. 1 Naval Postgraduate School Transonic Compressor Test Facility

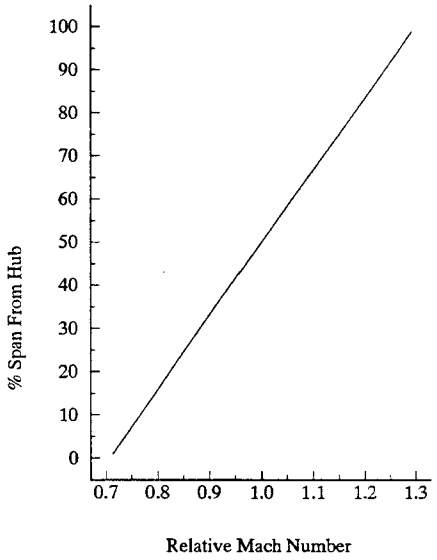

Fig. 3(a) Radial Distribution of Rotor Inlet Relative Mach Number

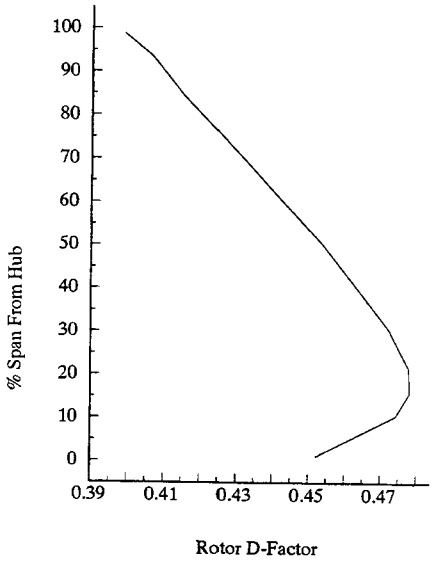

Fig. 3(b) Radial Distribution of Rotor D-Factor

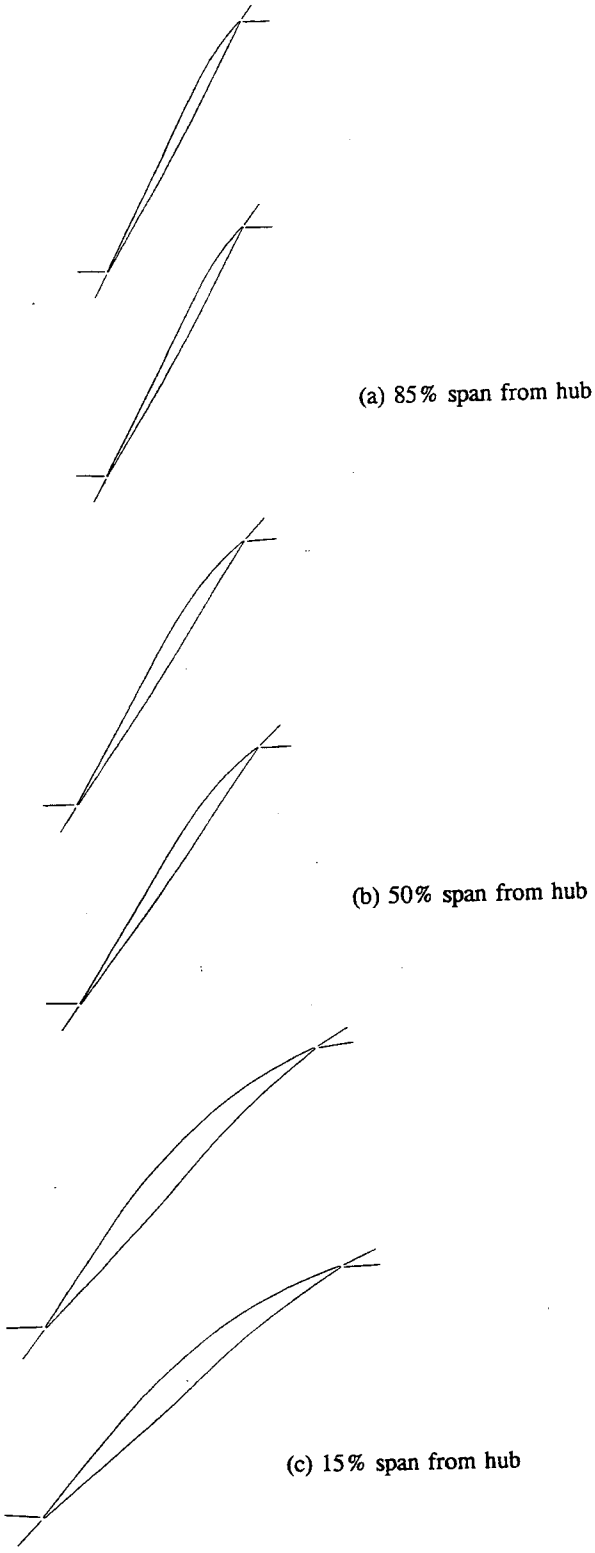

Fig. 4 Rotor Blade Sections

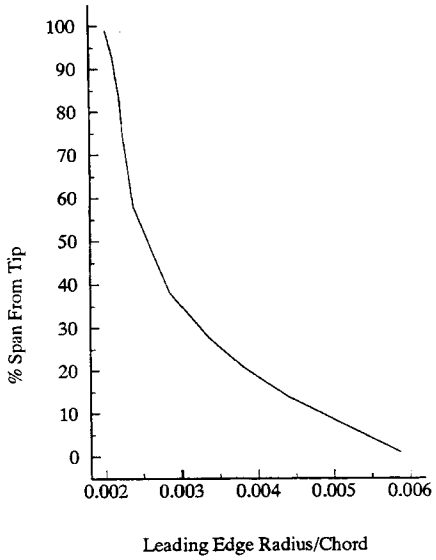

Fig. 5 Rotor Leading Edge Radius/Chord

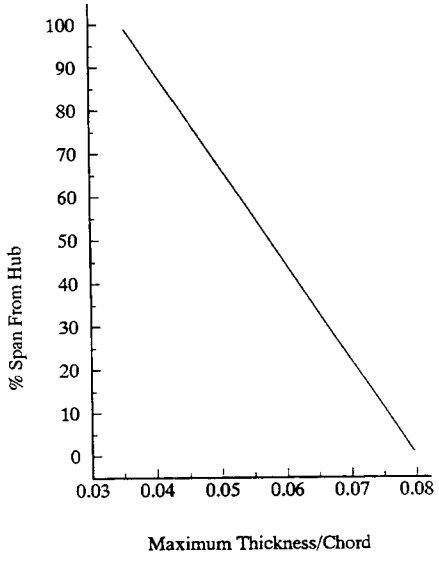

Fig. 6 Rotor Maximum Thickness/Chord

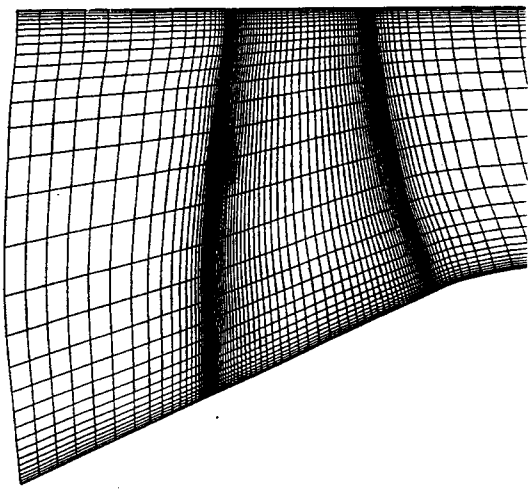

Fig. 7 Computational grid in the meridional plane

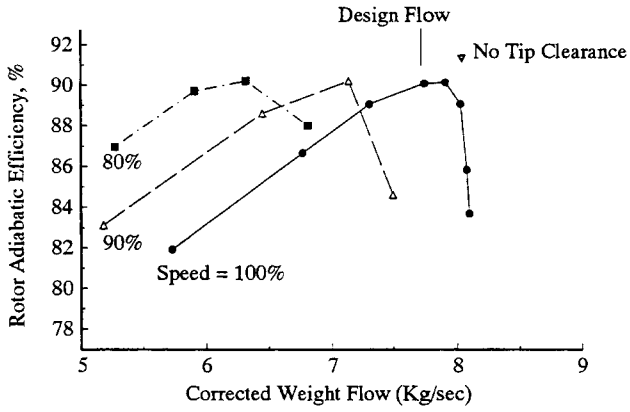

(a) Rotor Adiabatic Efficiency

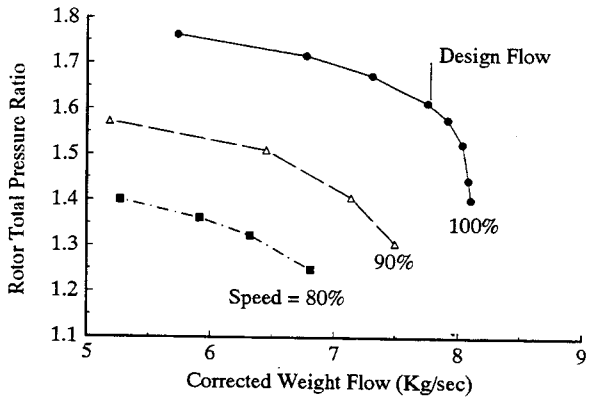

(b) Rotor Total Pressure Ratio

Fig. 8 Rotor performance map calculated with Denton TIP3D code

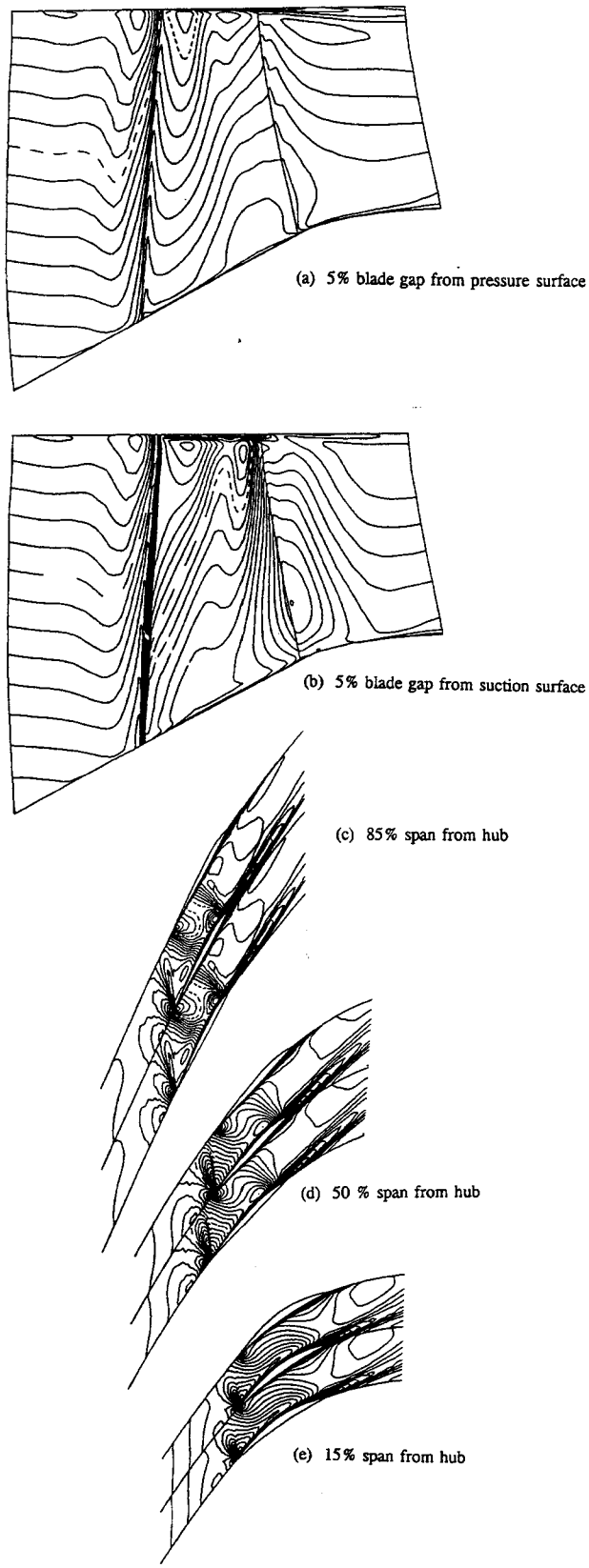

Fig. 9 Rotor relative Mach number at design flow

Mach No. increments - (a) and (b), 0.05
(c)-(e), 0.025, M' = 1.0 --------

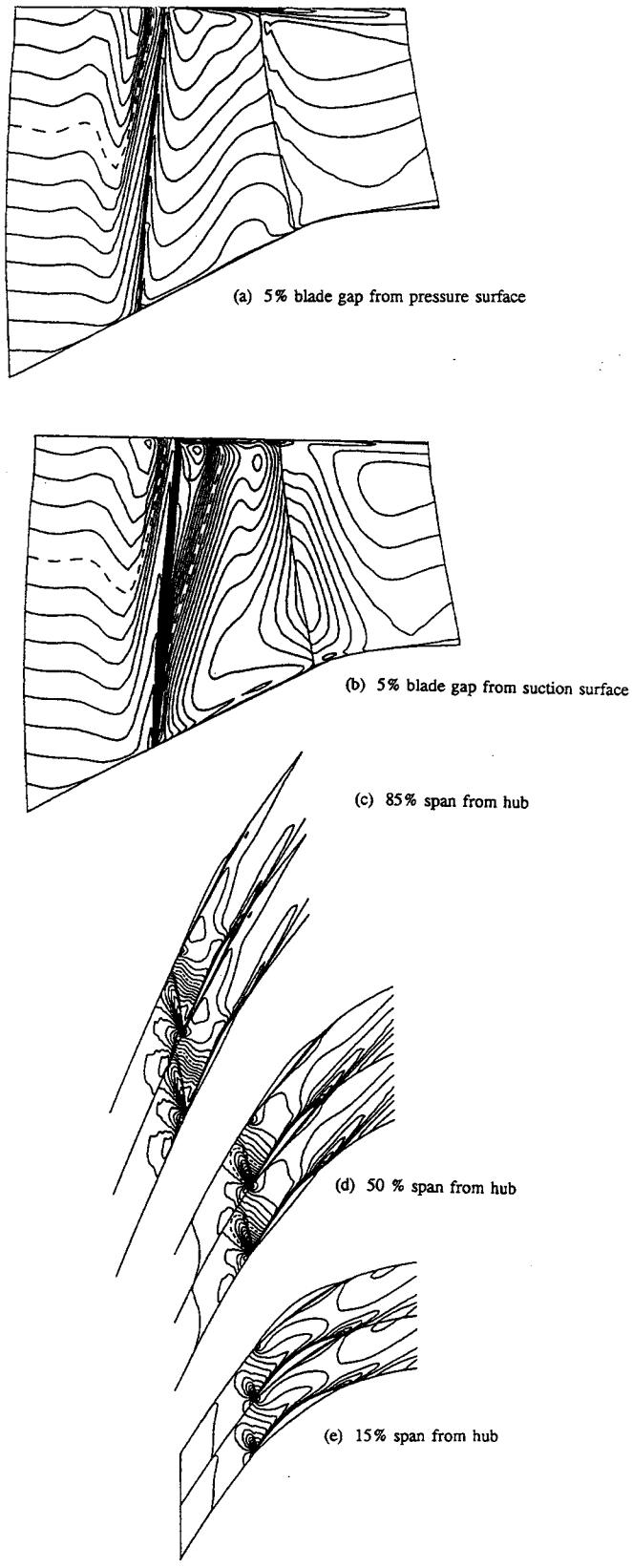

Fig. 10 Rotor relative Mach number at near stall flow

Mach number increments = 0.05
M' = 1.0 --------

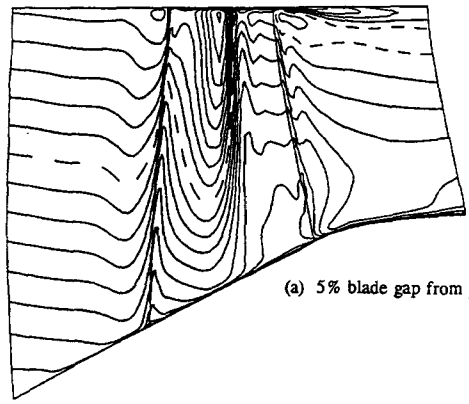

(a) 5% blade gap from pressure surface

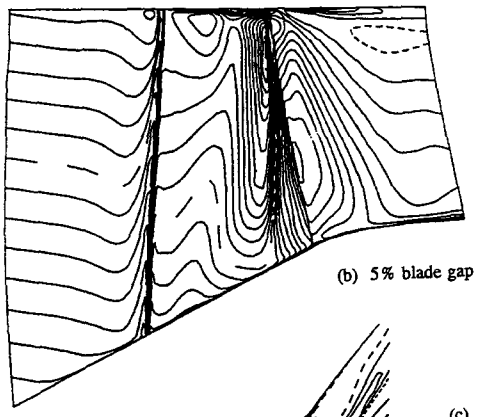

(b) 5% blade gap from suction surface

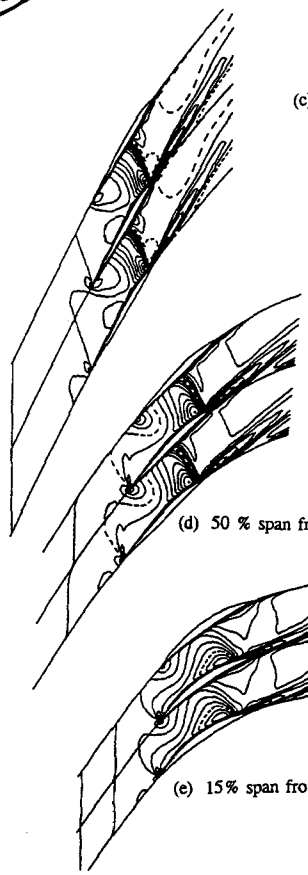

(c) 85% span from hub

(d) 50 % span from hub

(e) 15% span from hub

Fig. 11 Rotor relative Mach number at near choke flow

Mach no. increments = 0.05
M' = 1.0 --------

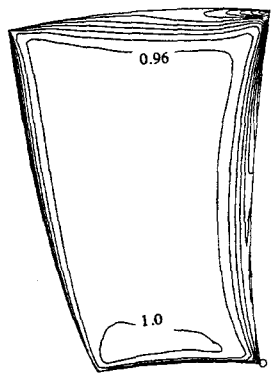

Fig. 12 Entropy function at 99.2% of rotor chord. Design flow. Entropy increments, 0.04.

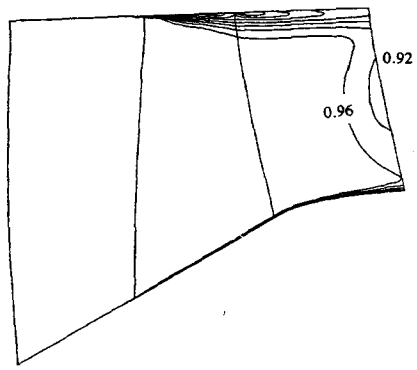

Fig. 13 Entropy function on mean meridional surface of rotor at design flow. Entropy increments, 0.04.

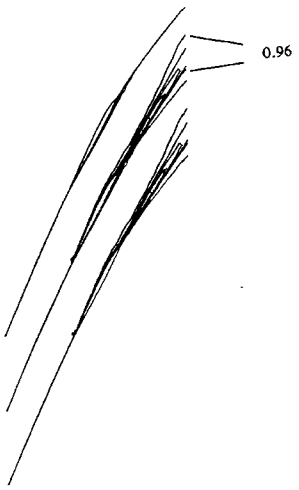

(a) 85% Span From Hub

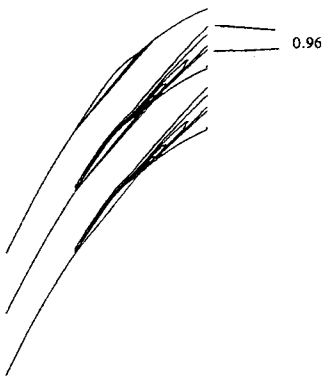

(b) 50% Span From Hub

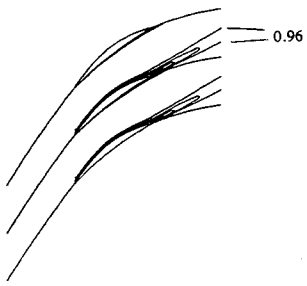

(c) 15% Span From Hub

Fig. 14 Entropy function on rotor blade-to-blade surfaces at design flow. Entropy increments, 0.04.

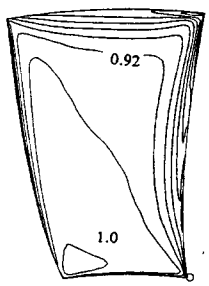

Fig. 15 Entropy function at 99.2% of rotor chord. Near stall flow. Entropy increments, 0.04.

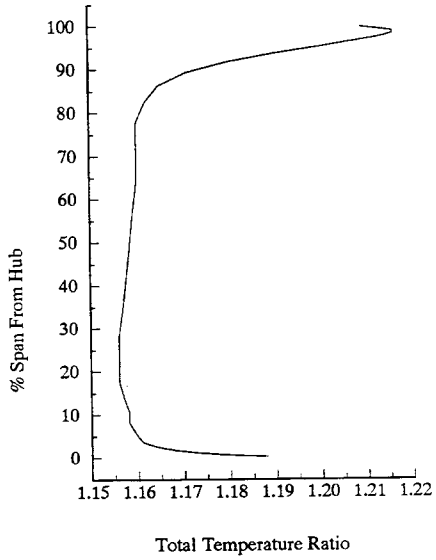

(a) Rotor Exit Total Temperature

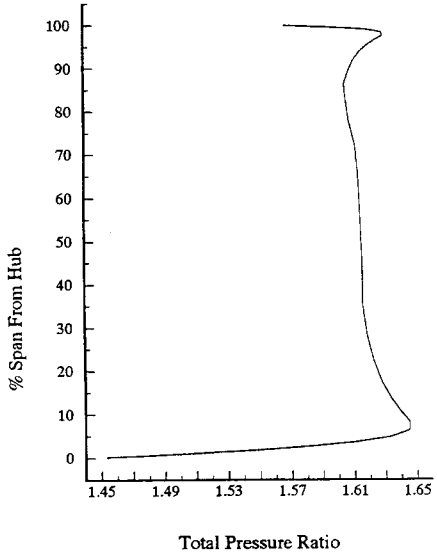

(b) Rotor Exit Total Pressure

Fig. 16 Radial distributions of rotor performance parameters at design flow

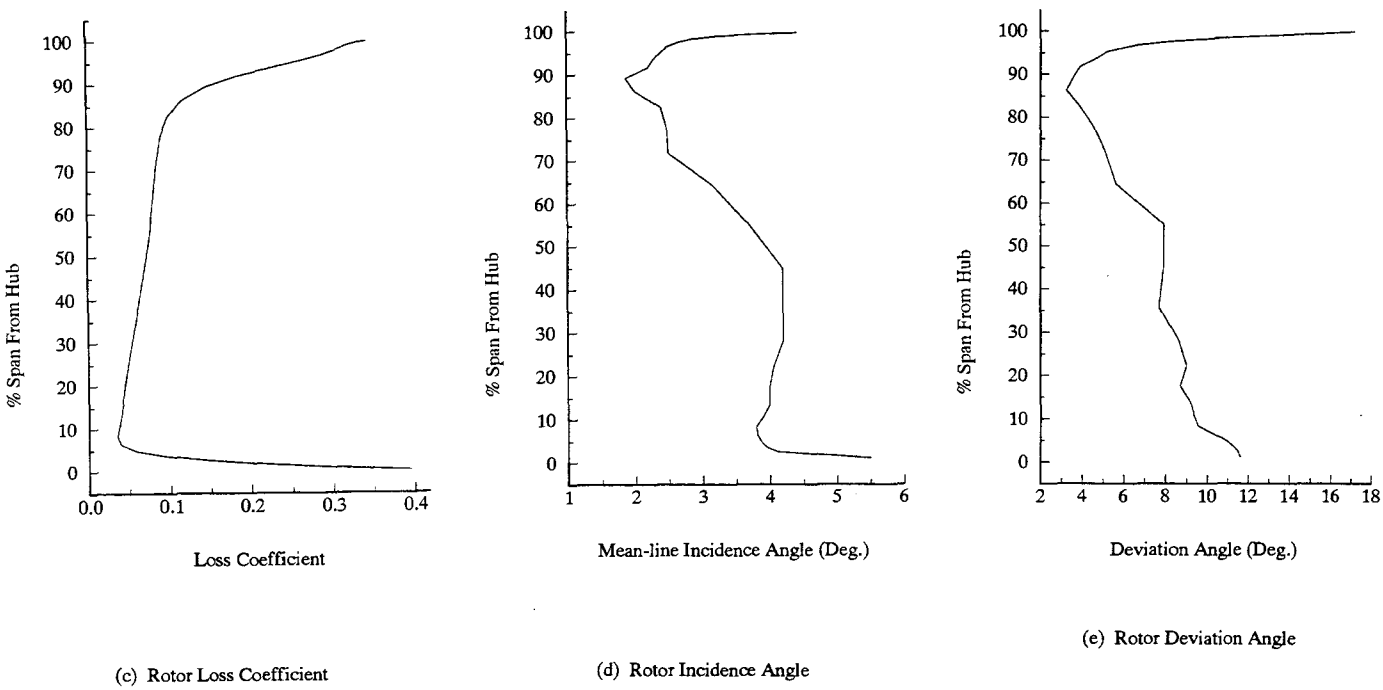

(c) Rotor Loss Coefficient

(d) Rotor Incidence Angle

(e) Rotor Deviation Angle

Fig. 16 Radial distributions of rotor performance parameters at design flow

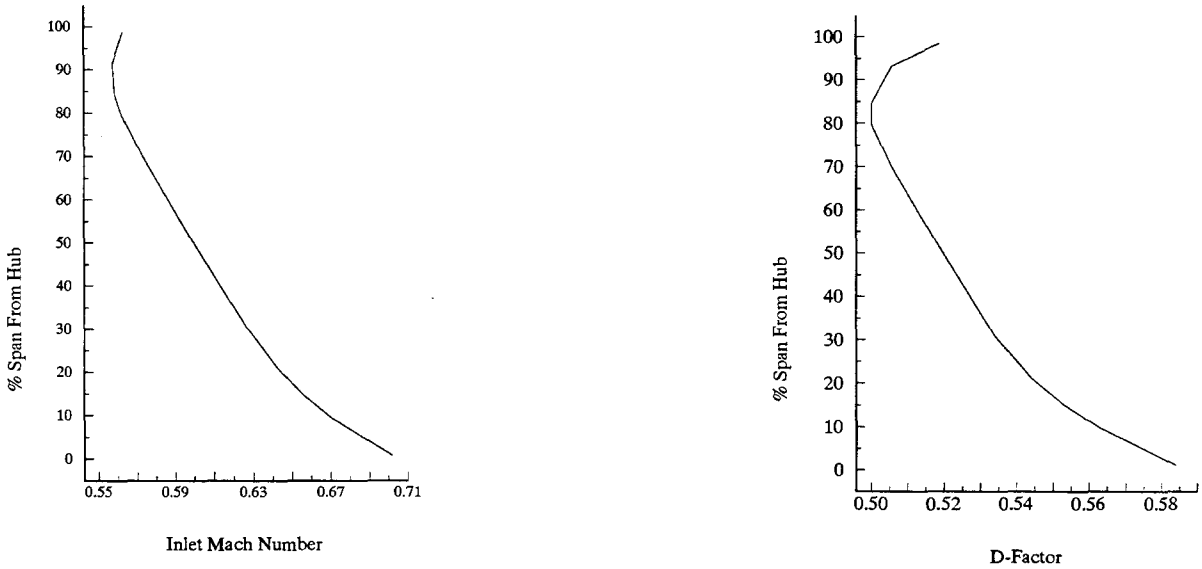

(a) Stator Inlet Mach Number

(b) Stator D-Factor

Fig. 17 Stator radial distributions of inlet Mach number and D-Factor

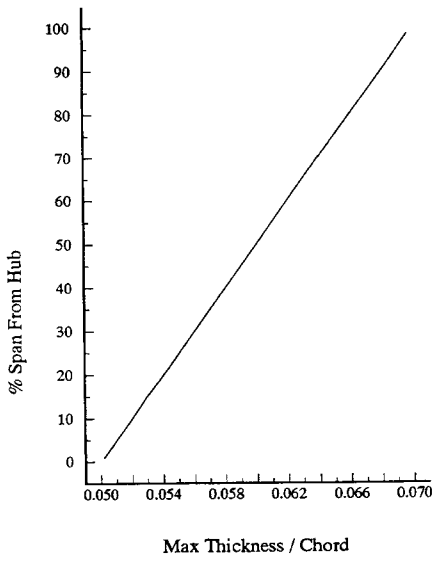

Fig. 18 Stator Maximum Thickness/Chord

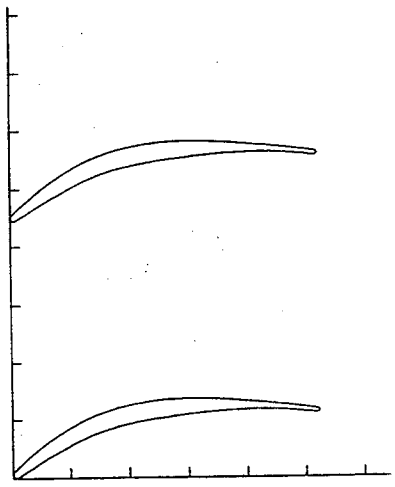

Fig. 19 Stator blade section at mid-span

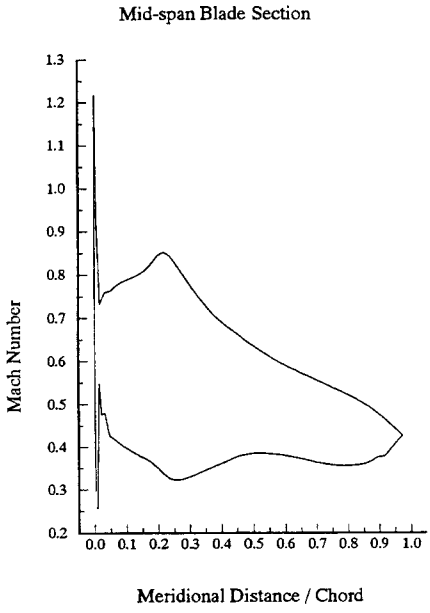

Fig. 20 Typical stator surface Mach number distribution

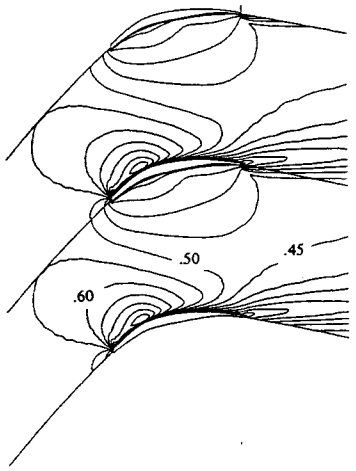

(a) 85% span from hub

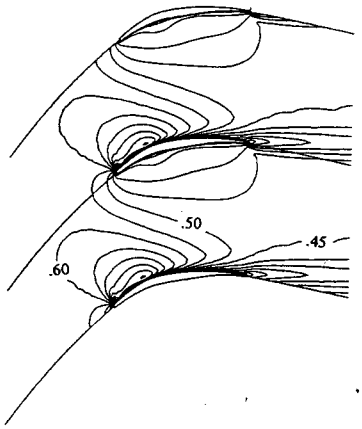

(b) 50% span from hub

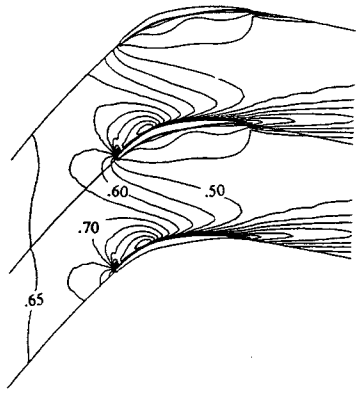

(c) 15% span from hub

Fig. 21 Absolute Mach numbers in the stator blade-to-blade planes at design flow. Mach number increments, 0.05.

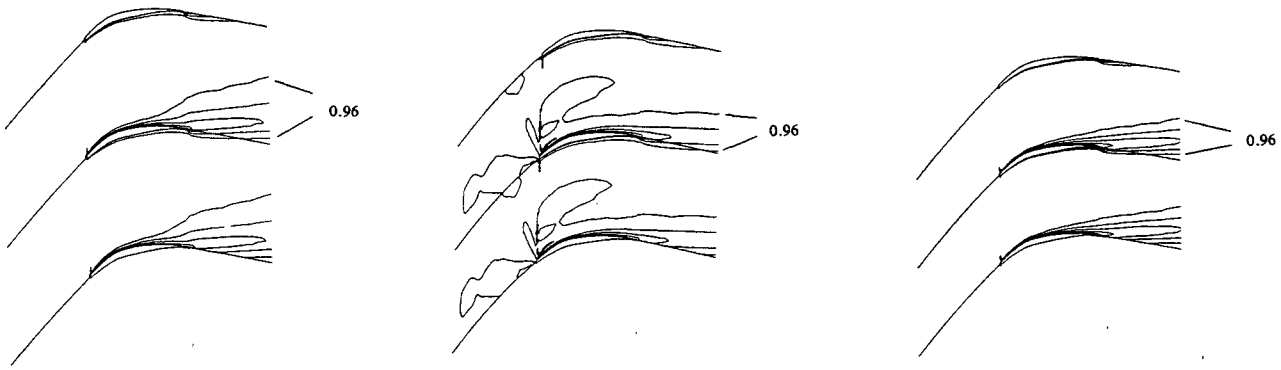

(a) 85% span from hub (b) 50% span from hub (c) 15% span from hub

Fig. 22 Entropy function in the stator bade-to-blade planes at design flow. Entropy increments, 0.04.

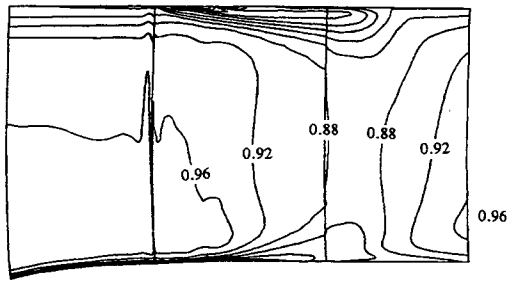

Fig. 22 Entropy function on the meridional plane at 5% blade gap from the suction surface. Design flow. Entropy increments, 0.04.

Fig. 24 Entropy function on the stator meridional plane at 5% blade gap from the suction surface. Design flow. Entropy increments, 0.04.

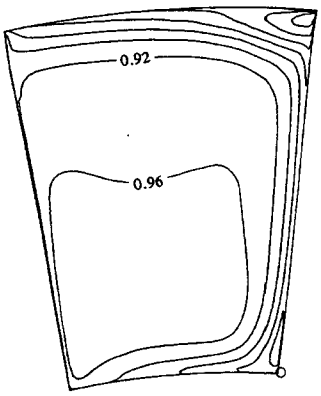

Fig. 23 Entropy function at 99.2% of stator chord. Design flow. Entropy increments, 0.04.

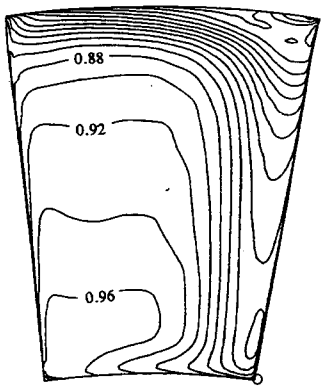

Fig. 25 Entropy function at 99.2% of stator chord. Near stall flow. Entropy increments, 0.02.

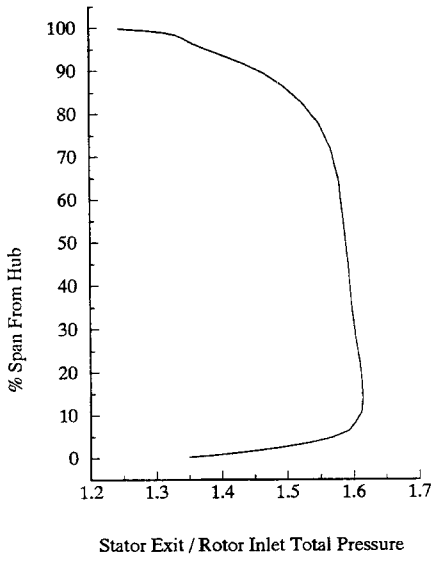

(a) Stator Exit Total Pressure

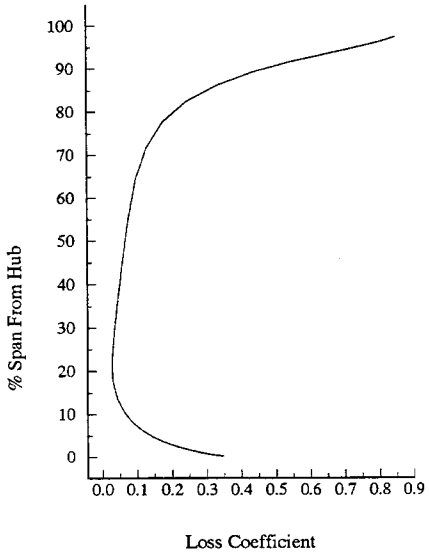

(b) Stator Loss Coefficient

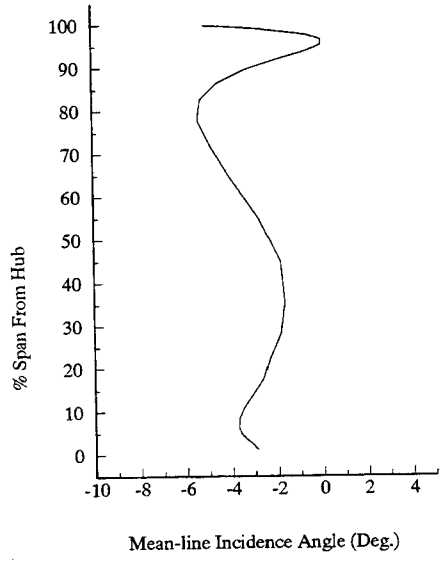

(c) Stator Incidence Angle

Fig. 26 Radial distribution of stator performance parameters at design flow

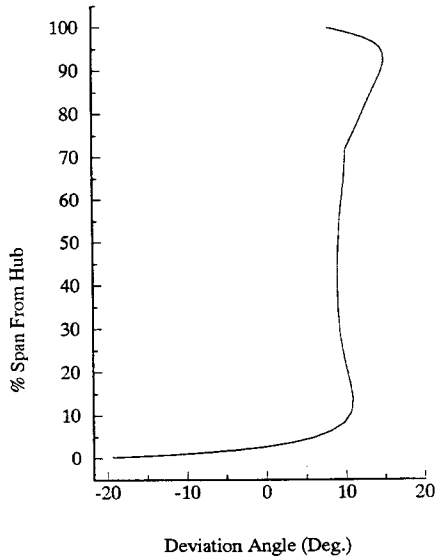

(d) Stator Deviation Angle

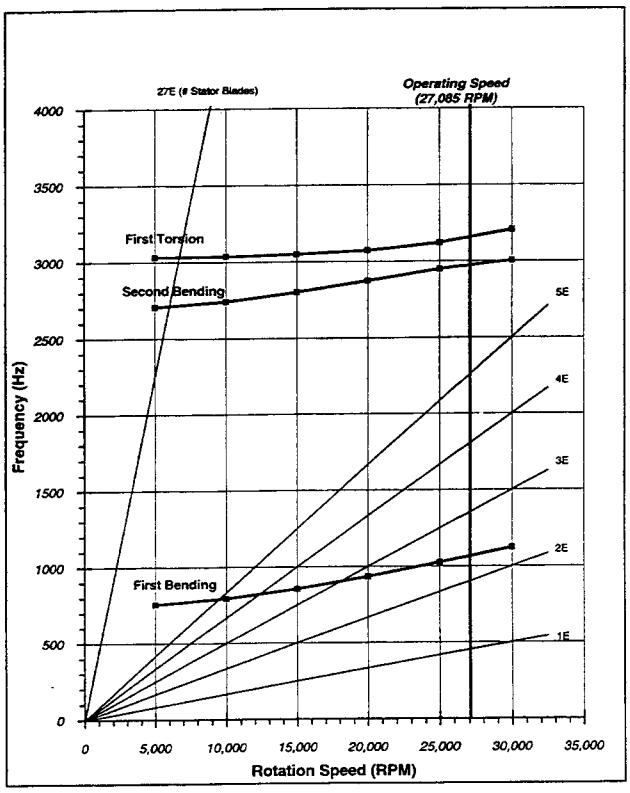

Fig. 27 Campbell diagram for rotor blades